Topological Boundary Modes in Isostatic Lattices

C. L. Kane and T. C. Lubensky
Dept. of Physics and Astronomy, University of Pennsylvania, Philadelphia, PA 19104

Frames, or lattices consisting of mass points connected by rigid bonds or central force springs, are important model constructs that have applications in such diverse fields as structural engineering, architecture, and materials science. The difference between the number of bonds and the number of degrees of freedom of these lattices determines the number of their zero-frequency "floppy modes". When these are balanced, the system is on the verge of mechanical instability and is termed isostatic. It has recently been shown that certain extended isostatic lattices exhibit floppy modes localized at their boundary. These boundary modes are insensitive to local perturbations, and appear to have a topological origin, reminiscent of the protected electronic boundary modes that occur in the quantum Hall effect and in topological insulators. In this paper we establish the connection between the topological mechanical modes and the topological band theory of electronic systems, and we predict the existence of new topological bulk mechanical phases with distinct boundary modes. We introduce model systems in one and two dimensions that exemplify this phenomenon.

Isostatic lattices provide a useful reference point for understanding the properties of a wide range of systems on the verge of mechanical instability, including network glasses[1,2], randomly diluted lattices near the rigidity percolation threshold[3,4], randomly packed particles near their jamming threshold[5–10], and biopolymer networks[11–14]. There are many periodic lattices, including the square and kagome lattices in $d = 2$ dimensions and the cubic and pyrochlore lattices in $d = 3$, that are locally isostatic with coordination number $z = 2d$ for every site under periodic boundary conditions. These lattices, which are the subject of this paper, have a surprisingly rich range of elastic responses and phonon structures[15–19] that exhibit different behaviors as bending forces or additional bonds are added.

The analysis of such systems dates to an 1864 paper by James Clerk Maxwell[20] that argued that a lattice with N_s mass points and N_b bonds has $N_0 = dN_s - N_b$ zero modes. Maxwell's count is incomplete, though, because N_0 can exceed $dN_s - N_b$ if there are $N_{\rm ss}$ states of self-stress, where springs can be under tension or compression with no net forces on the masses. This occurs, for example, when masses are connected by straight lines of bonds under periodic boundary conditions. A more general Maxwell relation[21],

$$\nu \equiv N_0 - N_{\rm ss} = dN_s - N_b, \tag{1}$$

is valid for infinitesimal distortions.

In a locally isostatic system with periodic boundary conditions, $N_0 = N_{\rm ss}$. The square and kagome lattices have one state of self-stress per straight line of bonds and associated zero modes along lines in momentum space. Cutting a section of N sites from these lattices removes states of self-stress and $\mathcal{O}(\sqrt{N})$ bonds and necessarily leads to $\mathcal{O}(\sqrt{N})$ zero modes, which are essentially identical to the bulk zero modes. Recently Sun *et al.*[22] studied a twisted kagome lattice in which states of self-stress are removed by rotating adjacent site sharing triangles in opposite directions. This simple modification gaps the bulk phonon spectrum (except for $\mathbf{q} = 0$) and localizes the required zero modes in the cut lattice to its surfaces.

These boundary zero modes are robust and insensitive to local perturbations. Boundary modes also occur in electronic systems, such as the quantum Hall effect[23,24] and topological insulators[25–30]. In this paper we establish the connection between these two phenomena. Our analysis allows us to predict the existence of new topologically distinct bulk mechanical phases and to characterize the protected modes that occur on their boundary. We introduce a 1D model that illustrates this phenomenon in its simplest form and maps directly to the Su-Schrieffer-Heeger (SSH) model[31]. We then prove an index theorem that generalizes equation (1) and relates the local count of zero modes on the boundary to the topological structure of the bulk. We introduce a deformed version of the kagome lattice model that exhibits distinct topological phases. The predictions of an index theorem are verified explicitly by solving for the boundary modes in this model. Finally, we show that some of the distinctive features of the topological phases can be understood within a continuum elastic theory.

Mechanical Modes and Topological Band Theory

A mechanical system of masses M connected by springs K is characterized by its equilibrium matrix[21] Q, which relates forces $F_i = Q_{im}T_m$ to spring tensions T_m. i labels the d components on the N_s sites and m labels the N_b bonds. Equivalently, $e_m = Q^T_{mi}u_i$ relates bond extensions e_m to site displacements u_i. The squared normal mode frequencies ω_n^2 are eigenvalues of the dynamical matrix $D = QQ^T$, where we set K/M to unity. The nullspace of Q^T describes the $N_0 = \dim\ker Q^T$ floppy modes. The nullspace of Q describes the $N_{\rm ss} = \dim\ker Q$ states of self-stress. The global counts of these two kinds of zero modes are related by the rank-nullity theorem[21], which may be expressed as an index theorem[32]. The index of Q, defined as $\nu = \dim\ker Q^T - \dim\ker Q$, is equal to the difference between the number of rows and columns of Q, and is given by equation (1).

At first sight, the mechanical problem and the quantum electronic problem appear different. Newton's laws are second-order equations in time, while the Schrodinger equation is first order. The eigenvalues of D are positive definite, while an elecronic Hamiltonian has positive and negative eigenvalues for the conduction and valence bands. To uncover the connection between the two problems we draw our inspiration from Dirac, who famously took the "square root" of the Klein Gordon equation[33]. To take the square root of the dynamical matrix, note that $D = QQ^T$ has a supersymmetric partner[34,35] $\tilde{D} = Q^T Q$ with the same non-zero eigenvalues. Combining D and $\tilde{D}$ gives a matrix that is a perfect square,

$$\mathcal{H} = \begin{pmatrix} 0 & Q \\ Q^T & 0 \end{pmatrix}; \quad \mathcal{H}^2 = \begin{pmatrix} QQ^T & 0 \\ 0 & Q^T Q \end{pmatrix}. \tag{2}$$

The spectrum of $\mathcal{H}$ is identical to that of D, except for the zero modes. Unlike D, the zero modes of $\mathcal{H}$ include *both* the zero modes of Q^T and Q, which are eigenstates of $\tau^z = \mathrm{diag}(1_{dN_s}, -1_{N_b})$ distinguished by their eigenvalue, ± 1.

Viewed as a Hamiltonian, $\mathcal{H}$ can be analyzed in the framework of topological band theory[29]. It has an intrinsic "particle-hole" symmetry, $\{\mathcal{H}, \tau^z\} = 0$, that guarantees eigenstates come in $\pm E$ pairs. Since Q_{im} is real, $\mathcal{H} = \mathcal{H}^*$ has "time-reversal" symmetry. These define symmetry class BDI[36]. In one-dimension, gapped Hamiltonians in this class are characterized by an integer topological invariant $n \in \mathbb{Z}$ that is a property of the Bloch Hamiltonian $\mathcal{H}(k)$ (or equivalently $Q(k)$) defined in the Brillouin zone (BZ). If bulk modes are all gapped, then $Q(k) \in GL_n$ is classified by an element of the homotopy group $\pi_1(GL_n) = \mathbb{Z}$, given by the winding number of the phase of $\det Q(k)$ around the BZ. A consequence is that a domain wall across which n changes is associated with topologically protected zero modes[31,37,38]. Below, we present an index theorem that unifies this bulk-boundary correspondence with equation (1) and shows how it can be applied to d-dimensional lattices, which form the analog of weak topological insulators[28].

Topological edge modes have been previously predicted in 2D photonic[39,40] and phononic[41] systems. These differ from the present theory because they occur in systems with bandgaps at finite frequency and broken time-reversal symmetry (symmetry class A). Localized end modes were found in a time-reversal invariant 1D model (class AI)[42]. However, the presence of those finite frequency modes is not topologically guaranteed.

One-Dimensional Model

Before discussing the index theorem we introduce a simple 1D model that illustrates the topological modes in their simplest setting. Consider a 1D system of springs connecting masses constrained to rotate at a radius R about fixed pivot points. In Fig. 1a the spring lengths are set so that the equilibrium configuration is $\langle \theta_i \rangle = 0$. Fig. 1b shows a configuration with shorter springs with $\langle \theta_i \rangle = \bar{\theta}$. Expanding in deviations $\delta\theta_i$ about $\bar{\theta}$, the extension of spring m is $\delta\ell_m = Q^T_{mi}\delta\theta_i$, with $Q^T_{mi} = q_1(\bar{\theta})\delta_{m,i} + q_2(\bar{\theta})\delta_{m,i+1}$ and $q_{1(2)} = r\cos\bar{\theta}(r\sin\bar{\theta} \pm 1)/\sqrt{4r^2\cos^2\bar{\theta} + 1}$. The normal mode dispersion is $\omega(k) = |Q(k)|$, where $Q(k) = q_1 + q_2 e^{ik}$. When $\bar{\theta} = 0$, $q_1 = -q_2$, and there are gapless bulk modes near $k = 0$. For a finite system with N sites and $N-1$ springs there is a single extended zero mode, as required by equation (1). For $\bar{\theta} \neq 0$ the bulk spectrum has a gap. In this case, the zero mode required by equation (1) is localized at one end or the other, depending on the sign of $\bar{\theta}$. The $\bar{\theta} > 0$ and $\bar{\theta} < 0$ phases are topologically distinct in the sense that it is impossible to tune between the two phases without passing through a transition where the gap vanishes. The topological distinction is captured by the winding number of the phase of $Q(k)$, which is 1 (0) for $|q_1| < (>) |q_2|$.

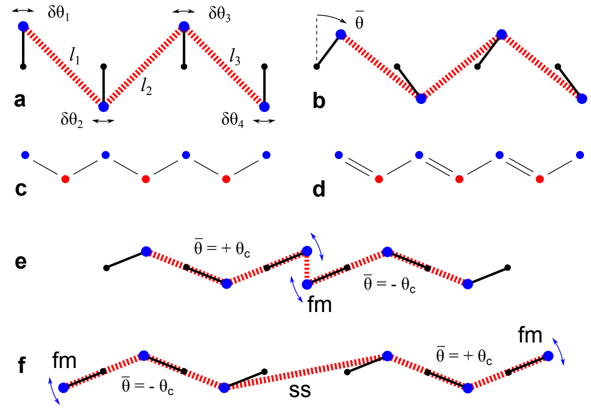

FIG. 1: **A one dimensional isostatic model system.** For $\bar{\theta} = 0$ **a** the vibrational spectrum is gapless, while for $\bar{\theta} > 0$ **b** there is a gap. **c** and **d** depict the SSH models corresponding to **a** and **b**. **e** shows a domain wall between $\bar{\theta} = +\theta_c$ and $-\theta_c$ in which the floppy mode at the interface is apparent. **f** shows the domain wall between $\bar{\theta} = -\theta_c$ and $+\theta_c$, with floppy modes at the ends and a state of self-stress at the interface.

Viewed as a quantum Hamiltonian, equation (2) for this model is identical to the SSH model[31], as indicated in Fig. 1(c,d). The sites and the bonds correspond, respectively, to the A and B sublattices of the SSH model. For $\bar{\theta} = 0$ the bonds in the SSH model are the same (Fig. 1c), while for $\bar{\theta} \neq 0$ they are dimerized (Fig. 1d). The two topological phases correspond to the two dimerization patterns for polyacetalene. As is well known for the SSH model[31,37], an interface between the two dimerizations binds a zero mode. This is most easily seen for $\bar{\theta} = \pm\theta_c$ where the springs are colinear with the bars, so that q_1 or $q_2 = 0$. Fig. 1e shows a domain wall between $+\theta_c$ and $-\theta_c$, in which the center two sites share a localized floppy mode. Fig. 1f shows an interface between $-\theta_c$ and $+\theta_c$ with a state of self-stress localized to the middle three bonds, in addition to floppy modes localized at either end. As long as there is a bulk gap, the zero modes cannot disappear when $\bar{\theta}$ deviates from $\pm\theta_c$. The zero modes remain exponentially localized, with a localization length that diverges when $\bar{\theta} \to 0$.

Index Theorem

There appear to be two distinct origins for zero modes. In equation (1) they arise because of a mismatch between the number of sites and bonds, while at a domain wall they arise in a location where there is no local mismatch. To unify them, we generalize the index theorem so that it determines the zero-mode count ν^S in a subsystem S of a larger system. This is well defined provided the boundary of S is deep in a gapped phase where zero modes are absent. We will show there are two contributions,

$$\nu^S = \nu_L^S + \nu_T^S, \tag{3}$$

where ν_L^S is a local count of sites and bonds in S and ν_T^S is a topological count, which depends on the topological structure of the gapped phases on the boundary of S.

To prove equation (3) and to derive formulas for ν_T^S and ν_L^S, we adapt a local version of the index theorem originally introduced by Callias[43–46] to allow for the possibility of non-zero ν_L^S. The details of the proof are given in the supplementary material. Here we will focus on the results. Consider a d-dimensional system described by a Hamiltonian $\mathcal{H}_{\alpha\beta}$, where α labels a site or a bond centered on $\mathbf{r}_\alpha$. The count of zero modes in S may be written

$$\nu^S = \lim_{\epsilon\to 0} \mathrm{Tr}\left[\tau^z \rho_S(\hat{\mathbf{r}}) \frac{i\epsilon}{\mathcal{H}+i\epsilon}\right], \tag{4}$$

where $\hat{\mathbf{r}}_{\alpha\beta} = \delta_{\alpha\beta}\mathbf{r}_\alpha$. The region S is defined by the support function $\rho^S(\mathbf{r}) = 1$ for $\mathbf{r} \in S$ and 0 otherwise. It is useful to consider $\rho^S(\mathbf{r})$ to vary smoothly between 1 and 0 on the boundary ∂S. Expanding the trace in terms of eigenstates of $\mathcal{H}$ shows that only zero modes with support in S contribute.

In the supplementary material we show that equation (4) can be rewritten as equation (3) with

$$\nu_L^S = \mathrm{Tr}\left[\rho^S(\hat{\mathbf{r}})\tau^z\right] \tag{5}$$

and

$$\nu_T^S = \int_{\partial S} \frac{d^{d-1}S}{V_{\rm cell}} \mathbf{R}_T \cdot \hat{n}, \tag{6}$$

where the integral is over the boundary of S with inward pointing normal $\hat{n}$. $\mathbf{R}_T = \sum_i n_i \mathbf{a}_i$ is a Bravais lattice vector characterizing the periodic crystal in the boundary region that can be written in terms of primitive vectors $\mathbf{a}_i$ and integers

$$n_i = \frac{1}{2\pi i}\oint_{C_i} d\mathbf{k}\cdot \mathrm{Tr}[Q(\mathbf{k})^{-1}\nabla_{\mathbf{k}} Q(\mathbf{k})]. \tag{7}$$

Here C_i is a cycle of the BZ connecting $\mathbf{k}$ and $\mathbf{k}+\mathbf{b}_i$, where $\mathbf{b}_i$ is a primitive reciprocal vector satisfying $\mathbf{a}_i\cdot\mathbf{b}_j = 2\pi\delta_{ij}$. n_i are winding numbers of the phase of $\det Q(\mathbf{k})$ around the cycles of the BZ, where $Q(\mathbf{k})$ is the equilibrium matrix in a Bloch basis.

To apply equations (6) and (7), it is important that the winding number be independent of path. This is the case if there is a gap in the spectrum. We will also apply this when the gap vanishes for acoustic modes at $\mathbf{k} = 0$. This is okay because the acoustic mode is not topological in the sense that it can be gapped by a weak translation symmetry breaking perturbation. This means the winding number is independent of $\mathbf{k}$ even near $\mathbf{k} = 0$. It is possible, however, that there can be topologically protected gapless points. These would be point zeros around which the phase of $\det Q(\mathbf{k})$ advances by 2π. These lead to topologically protected bulk modes that form the analog of a "Dirac semimetal" in electronic systems like graphene. These singularities could be of interest, but they do not occur in the model we study below.

A second caveat for equation (7) is that, in general, the winding number is not gauge invariant and depends on how the sites and bonds are assigned to unit cells. In the supplementary material we show that for an isostatic lattice with uniform coordination it is possible to adopt a "standard unit cell" with basis vectors $\mathbf{d}_{i(m)}$ for the n_s sites (dn_s bonds) per cell that satisfy $\mathbf{r}_0 = d\sum_i \mathbf{d}_i - \sum_m \mathbf{d}_m = 0$. $Q(\mathbf{k})$ is defined using Bloch basis states $|\mathbf{k}, a = i, m\rangle \propto \sum_{\mathbf{R}} \exp i\mathbf{k}\cdot(\mathbf{R}+\mathbf{d}_a)|\mathbf{R}+\mathbf{d}_a\rangle$, where $\mathbf{R}$ is a Bravais lattice vector. In this gauge, $\mathbf{R}_T$ is uniquely defined and the zero-mode count is given by equations (3) and (5)-(7).

To determine the number of zero modes per unit cell on an edge indexed by a reciprocal lattice vector $\mathbf{G}$, consider a cylinder with axis perpendicular to $\mathbf{G}$ and define the region S to be the points nearest to one end of the cylinder (See Supplementary Fig. 1). ν_T^S is determined by evaluating equation (6) on ∂S deep in the bulk of the cylinder. It follows that

$$\tilde{\nu}_T \equiv \nu_T^S/N_{\rm cell} = \mathbf{G}\cdot\mathbf{R}_T/2\pi. \tag{8}$$

The local count, ν_L^S, depends on the details of the termination at the surface and can be determined by evaluating the macroscopic "surface charge" that arises when charges $+d$ (-1) are placed on the sites (bonds) in a manner analogous to the "pebble game"[4]. This can be found by defining a bulk unit cell with basis vectors $\tilde{\mathbf{d}}_a$ that accommodate the surface with no leftover sites or bonds (see Fig. 4a below). Note that this unit cell depends on the surface termination and, in general, will be different from the "standard" unit cell used for ν_T^S. The local count is then the surface polarization charge given by the dipole moment per unit cell. We find

$$\tilde{\nu}_L \equiv \nu_L^S/N_{\rm cell} = \mathbf{G}\cdot\mathbf{R}_L/2\pi, \tag{9}$$

where

$$\mathbf{R}_L = d\sum_{\text{sites } i}\tilde{\mathbf{d}}_i - \sum_{\text{bonds } m}\tilde{\mathbf{d}}_m. \tag{10}$$

$\mathbf{R}_L$ is similar to $\mathbf{r}_0$ defined above (which is assumed to be zero), but it is in general a different Bravais lattice vector. The total zero mode count on the surface then follows from equations (3), (8), and (9).

Deformed Kagome Lattice Model

We now illustrate the topological boundary modes of a two-dimensional lattice with the connectivity of the kagome lattice, but with deformed positions. The deformed kagome lattice is specified by its Bravais lattice and basis vectors for the three atoms per unit cell. For simplicity, we fix the Bravais lattice to be hexagonal with primitive vectors $\mathbf{a}_{p+1} = (\cos 2\pi p/3, \sin 2\pi p/3)$. We parameterize the basis vectors as $\mathbf{d}_1 = \mathbf{a}_1/2 + \mathbf{s}_2$, $\mathbf{d}_2 = \mathbf{a}_2/2 - \mathbf{s}_1$ and $\mathbf{d}_3 = \mathbf{a}_3/2$. Defining $\mathbf{s}_3 = -\mathbf{s}_1 - \mathbf{s}_2$, $\mathbf{s}_p$ describe the displacement of $\mathbf{d}_{p-1}$ relative to the midpoint of the line along $\mathbf{a}_p$ that connects its neighbors at $\mathbf{d}_{p+1} \pm \mathbf{a}_{p\mp 1}$ (with p defined mod 3), as indicated in Fig. 2a. $\mathbf{s}_p$ are specified by 6 parameters with 2 constraints. A symmetrical representation is to take

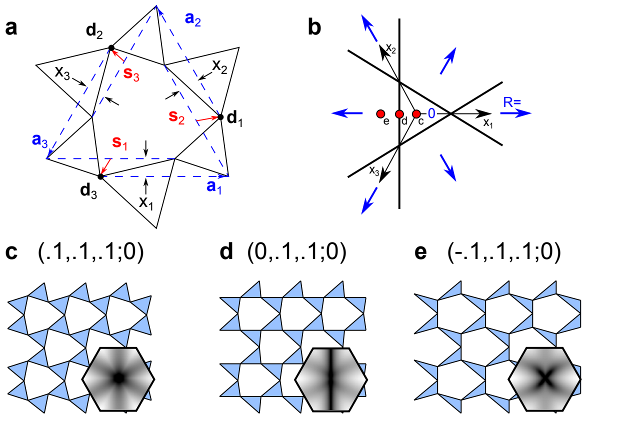

FIG. 2: **Deformed kagome lattice model.** **a** shows our convention for labeling the states. **b** is a ternary plot of the phase diagram for fixed $x_1 + x_2 + x_3 > 0$. The phases are labled by $\mathbf{R}$, which is zero in the central phase and a nearest neighbor lattice vector in the other phases. **c**, **d** and **e** show representative structures for $\mathbf{R} = 0$ (**c**) and $\mathbf{R} \neq 0$ (**e**) and the transition between them (**d**). The insets are density plots of the smallest mode frequency as a function of $\mathbf{k}$ in the BZ. In **c** the gap vanishes only at $\mathbf{k} = 0$, while in **d** it vanishes on the line $k_x = 0$. In **e** the gap vanishes only at $\mathbf{k} = 0$, but has a quadratic dependence in some directions for small $\mathbf{k}$.

$\mathbf{s}_p = x_p(\mathbf{a}_{p-1} - \mathbf{a}_{p+1}) + y_p\mathbf{a}_p$ and to use independent variables $(x_1, x_2, x_3; z)$ with $z = y_1 + y_2 + y_3$. The constraints then determine $y_p = z/3 + x_{p-1} - x_{p+1}$. x_p describes the buckling of the line of bonds along $\mathbf{a}_p$, so that when $x_p = 0$ the line of bonds is straight. z describes the asymmetry in the sizes of the two triangles. $(0, 0, 0; 0)$ is the undistorted kagome lattice, while $(x, x, x; 0)$ is the twisted kagome lattice, studied in[22], with twist angle $\theta = \tan^{-1}(2\sqrt{3}x)$.

It is straightforward to solve for the bulk normal modes of the periodic lattice. When any of the x_p are zero the gap vanishes on the line $\mathbf{k} \cdot \mathbf{a}_p = 0$ in the BZ. This line of zero modes is a special property of this model that follows from the presence of straight lines of bonds along $\mathbf{a}_p$. When $x_p = 0$ the system is at a critical point separating topologically distinct bulk phases. The phase diagram features the eight octants specified by the signs of $x_{1,2,3}$. $(+ + +)$ and $(- - -)$ describe states topologically equivalent to the twisted kagome lattice. The remaining 6 octants are states that are topologically distinct, but are related to each other by C_6 rotations. We find

$$\mathbf{R}_T = \sum_{p=1}^{3} \mathbf{a}_p \mathrm{sgn} x_p/2 \tag{11}$$

is independent of z. Fig. 2b shows a ternary plot of the phase diagram as a function of x_1, x_2, x_3 for $z = 0$ and a fixed value of $x_1 + x_2 + x_3$. Fig. 2c,d,e show representative structures for the $\mathbf{R}_T = 0$ phase (Fig. 2c), the $\mathbf{R}_T \neq 0$ phase (Fig. 2e), and the transition between them (Fig. 2d). The insets show density plots of the lowest frequency mode, which highlight the gapless point due to the acoustic mode in Fig. 2c and the gapless line in Fig. 2d. In Fig. 2e, the gap vanishes only at the origin, but the cross arises because acoustic modes vary quadratically rather than linearly with $\mathbf{k}$ along its axes. This behavior will be discussed in the next section.

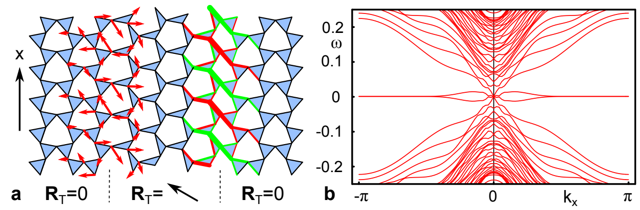

FIG. 3: **Zero modes at a domain wall.** **a** shows a lattice with periodic boundary conditions and a domain wall between $(.1, .1, .1, 0)$ and $(-.1, .1, .1, 0)$, and indicates the zero mode eigenvectors at $k_x = \pi$ for the floppy mode (arrows) and the state of self-stress (red (+) and green (-) thickened bonds). **b** shows the vibrational mode dispersion as a function of k_x.

We next examine the boundary modes of the deformed kagome lattice. Fig. 3 shows a system with periodic boundary conditions in both directions that has domain walls separating $(.1, .1, .1; 0)$ from $(-.1, .1, .1; 0)$. Since there are no broken bonds, the local count is $\nu_S^L = 0$. On the two domain walls, equation (8) predicts $\tilde{\nu}_T = +1(-1)$ for the left (right) domain wall. Fig. 2c shows the spectrum of $\mathcal{H}$ (which has both positive and negative eigenvalues) as a function of the momentum k_x parallel to the domain wall. The zero modes of $\mathcal{H}$ include both the floppy modes and the states of self-stress. In the vicinity of $k_x = 0$ the zero modes on the two domain walls couple and split because their penetration depth diverges as $k_x \to 0$. The eigenvectors for the zero modes at $k_x = \pi$ are indicated in Fig. 3a by the arrows and the thickened bonds.

Fig. 4a shows a segment of a $(-.05, .05, .05; 0)$ lattice with three different different edges. For each edge, a unit cell that accommodates the edge is shown, along with the corresponding $\mathbf{R}_L$, from which $\tilde{\nu}_L$ is determined. In the interior, a "standard" unit cell, with $\mathbf{r}_0 = 0$ is shown. Figs. 4b, c, d show the spectrum for a strip with one edge given by the corresponding edge in Fig. 4a with free boundary conditions. The other edge of the strip is terminated with clamped boundary conditions, so that the floppy modes are due solely to the free edge. The number of zero modes per unit cell agrees with equations (8) and (9) for each surface given $\mathbf{R}_L$, $\mathbf{R}_T$. The zero modes acquire a finite frequency when the penetration length of the zero mode approaches the strip width, which leads to Gaussian "bumps" near $k = 0$, which will be discussed in the next section. In Fig. 4d, one of the three zero modes can be identified as a localized "rattler", which remains localized on the surface sites, even for $k \to 0$.

Continuum Elasticity Theory

Unlike electronic spectra, phonon spectra have acoustic modes whose frequencies vanish as $\mathbf{k} \to 0$. These excitations along with macroscopic elastic distortions and long-wavelength surface Rayleigh waves are described by a continuum elastic energy quadratic in the elastic strain tensor u_{ij}. The elastic energies of our model isostatic lattices fall into distinct classes depending on the topological class of the lat-

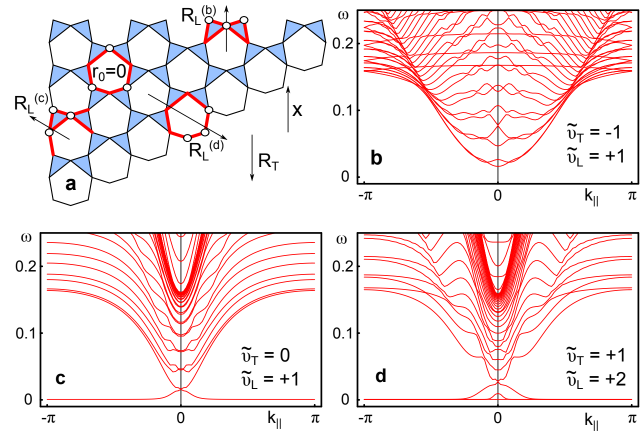

FIG. 4: **Zero modes at the edge.** **a** shows a $(-.05, .05, .05, 0)$ lattice indicating three edges. **b**, **c** and **d** show the vibrational mode spectrum computed for a strip with one edge as shown in **a** and the other edge with a clamped boundary condtion. The zero mode count on each surface is compared with equations (3,8,9).

tice even though they do not directly encode topological structure. For simplicity we focus on $(x_1, x_2, x_2; 0)$ states, where $x_2 > 0$ is fixed and x_1 is allowed to vary. The elastic energy density f can be written

$$f = \frac{K}{2}[(u_{xx} - a_1 u_{yy})^2 + 2a_4 u_{xy}^2 - 2a_5(u_{xx} - a_1 u_{yy})u_{xy}]. \quad (12)$$

We find that $a_{1,5} \propto x_1$ for small x_1, while $a_4 > 0$ is constant. Thus, the $\mathbf{R}_T = 0$ and $\mathbf{R}_T \neq 0$ sectors are distinguished by the signs of $a_{1,5}$. $f = 0$ for shape distortions with $u_{xx} = a_1 u_{yy}$ and $u_{xy} = 0$. When $a_1 > 0$, the distortion has a negative Poisson ratio[47], expanding or contracting in orthogonal directions (a feature shared by the twisted kagome lattice[22]); when $a_1 < 0$, the distortion has the more usual positive Poisson ratio. Finally when $a_1 = 0$, uniaxial compressions along y costs no energy.

Expanding $\det Q^T$ for small $\mathbf{k}$ provides useful information about the bulk- and surface-mode structure. To order k^3,

$$\det Q^T = A[k_x^2 + a_1 k_y^2 + ic(k_x^3 - 3k_x k_y^2)] + O(k^4), \quad (13)$$

where $A, c > 0$ for small x_1. a_1 is the same as in equation (12). Long-wavelength zero modes are solutions of $\det Q^T = 0$. The quadratic term, which corresponds to the elastic theory, equation (12), reveals an important difference between the bulk acoustic modes of $\mathbf{R}_T = 0$ and $\mathbf{R}_T \neq 0$. In the former case, $a_1 > 0$, $\det Q^T = 0$ only at $\mathbf{k} = 0$. For $a_1 < 0$, though, to order k^2, $\det Q^T = 0$ for $k_x = \pm\sqrt{|a_1|}k_y$, so the elastic theory predicts lines of gapless bulk modes. The degeneracy is lifted by the k^3 term, leading to a k^2 dispersion along those lines, which can be seen by the cross in the density map of Fig. 2e.

$\det Q^T(\mathbf{k} \to 0)$ vanishes for complex wavenumbers associated with zero-frequency Rayleigh surface waves. Writing $\mathbf{k} = k_\perp \hat{n} + k_{||}\hat{z} \times \hat{n}$ for a surface whose outward normal $\hat{n}$ makes an angle θ with $\hat{x}$, there is an $\omega = 0$ Rayleigh wave with penetration depth $|\mathrm{Im}\, k_\perp|^{-1}$ if $\mathrm{Im}\, k_\perp < 0$. To order $k_{||}^2$ there are two solutions,

$$k_\perp^\pm = \frac{\sin\theta \pm i\sqrt{a_1}\cos\theta}{\cos\theta \mp i\sqrt{a_1}\sin\theta} k_{||} + \frac{i(3 + a_1)d}{2(\cos\theta \pm i\sqrt{a_1}\sin\theta)^3} k_{||}^2. \quad (14)$$

When $a_1 > 0$, the linear term is always finite and nonzero, and $\mathrm{Im}\, k_\perp^\pm$ have opposite signs, indicating that there can be acoustic surface zero modes on all surfaces. These are the classical Rayleigh waves predicted by the elastic theory, with penetration depth $\mathcal{O}(k_{||}^{-1})$. When $a_1 < 0$, the linear term in $k_{||}$ is real and $\mathrm{Im}\, k_\perp^\pm \propto k_{||}^2$. The number of long wavelength surface zero modes depends on the angle of the surface. When $|\theta| < \theta_c = \cot^{-1}\sqrt{|a_1|}$, $\mathrm{Im}\, k_\perp^\pm$ are both positive, and there are no acoustic surface zero modes. The opposite surface, $|\theta - \pi| < \theta_c$, has two acoustic surface modes. For $\theta_c < \theta < \pi - \theta_c$ $\mathrm{Im}\, k_\perp^\pm$ have opposite sign, so there is one mode. This is consistent with the mode structure in Fig. 4: The $\mathcal{O}(k_{||}^{-2})$ penetration depth explains the Gaussian profile of the $k \to 0$ bumps in the zero modes, which are due to the finite strip width. In (b) a $\theta = 0$ surface has no zero modes. (c) shows a $\theta = \pi/2 > \theta_c$ surface with one long-wavelength surface zero mode. (d) shows the spectrum with $\pi - \theta = \pi/6 < \theta_c$ with two bumps indicating two deeply penetrating long-wavelength zero modes in addition to one non-acoustic mode localized at that surface.

Conclusions

We have developed a general theory of topological phases of isostatic lattices, which explains the boundary zero modes and connects to the topological band theory of electronic systems. This points to several directions for future studies. It will be interesting to study 3D lattice models, as well as lattices that support point singularities in $\det Q(\mathbf{k})$ analogous to Dirac semimetals. Finally, it will be interesting to explore connections with theories of frustrated magnetism[48].

Acknowledgments

TCL is grateful for the hospitality of the Newton Institute, where some of this work was carried out. This work was supported in part by a Simons Investigator award to CLK from the Simons Foundation and by the National Science Foundation under DMR-1104707 (TCL) and DMR-0906175 (CLK).

[1] Phillips, J. C. Topology of Covalent Non-Crystalline Solids 2. Medium-Range Order in Chalcogenide Alloys and $\alpha -$ Si((Ge). *Journal of Non-Crystalline Solids* **43**, 37–77 (1981).

[2] Thorpe, M. F. Continuous Deformations in Random Networks. *Journal of Non-Crystalline Solids* **57**, 355–370 (1983).
[3] Feng, S. & Sen, P. N. Percolation on Elastic Networks - New Exponent and Threshold. *Physical Review Letters* **52**, 216–219 (1984).
[4] Jacobs, D. J. & Thorpe, M. F. Generic Rigidity Percolation - the Pebble Game. *Physical Review Letters* **75**, 4051–4054 (1995).
[5] Liu, A. J. & Nagel, S. R. Nonlinear dynamics - Jamming is not just cool any more. *Nature* **396**, 21–22 (1998).
[6] Liu, A. J. & Nagel, S. R. Granular and jammed materials. *Soft Matter* **6**, 2869–2870 (2010).
[7] Liu, A. J. & Nagel, S. R. The Jamming Transition and the Marginally Jammed Solid. *Annual Review of Condensed Matter Physics* **1**, 347–369 (2010).
[8] Torquato, S. & Stillinger, F. H. Jammed hard-particle packings: From Kepler to Bernal and beyond. *Reviews of Modern Physics* **82**, 2633–2672 (2010).
[9] Wyart, M., Nagel, S. R. & Witten, T. A. Geometric origin of excess low-frequency vibrational modes in weakly connected amorphous solids. *Europhysics Letters* **72**, 486–492 (2005).
[10] Wyart, M. On the rigidity of amorphous solids. *Annales De Physique* **30**, 1–96 (2005).
[11] Wilhelm, J. & Frey, E. Elasticity of stiff polymer networks. *Physical Review Letters* **91**, 108103 (2003).
[12] Heussinger, C. & Frey, E. Floppy modes and nonaffine deformations in random fiber networks. *Physical Review Letters* **97**, 105501 (2006).
[13] Huisman, L. & Lubensky, T. C. Internal stresses, normal modes and non-affinity in three-dimensional biopolymer networks. *Physical Review Letters* **106**, 088301 (2011).
[14] Broedersz, C., Mao, X., Lubensky, T. C. & MacKintosh, F. C. Criticality and isostaticity in fiber networks. *Nature Physics* **7**, 983–988 (2011).
[15] Souslov, A., Liu, A. J. & Lubensky, T. C. Elasticity and response in nearly isostatic periodic lattices. *Physical Review Letters* **103**, 205503 (2009).
[16] Mao, X. M., Xu, N. & Lubensky, T. C. Soft Modes and Elasticity of Nearly Isostatic Lattices: Randomness and Dissipation. *Physical Review Letters* **104**, 085504 (2010).
[17] Mao, X. M. & Lubensky, T. C. Coherent potential approximation of random nearly isostatic kagome lattice. *Physical Review E* **83**, 011111 (2011).
[18] Mao, X. M., Stenull, O. & Lubensky, T. C. Elasticity of a filamentous kagome lattice. *Physical Review E* **87**, 042602 (2013).
[19] Kapko, V., Treacy, M. M. J., Thorpe, M. F. & Guest, S. D. On the collapse of locally isostatic networks. *Proc. Royal Soc. A* **465**, 3517–3530 (2009).
[20] Maxwell, J. C. On the Calculaton of the Equilibirum Stiffness of Frames. *Philosophical Magazine* **27**, 294 (1865).
[21] Calladine, C. R. Buckminster Fuller's "Tensegrity" Structures and Clerk Maxwell's Rules for the Construction of Stiff Frames. *International Journal of Solids and Structures* **14**, 161–172 (1978).
[22] Sun, K., Mao, X. & Lubensky, T. C. Surface phonons, elastic response, and conformal invariance in twisted kagome lattices. *PNAS* **109**, 12369–12374 (2012).
[23] Halperin, B. I. Quantized Hall Conductance, Current-Carrying Edge States, and the Existence of Extended States in a Two-Dimensional Disordered Potential. *Physical Review B* **25**, 2185–2190 (1982).
[24] Haldane, F. D. M. Model for a Quantum Hall Effect Without Landau Levels - Condensed Matter Realization of the Parity Anomaly. *Physical Review Letters* **61**, 2015–2018 (1988).
[25] Kane, C. L. & Mele, E. J. Z(2) topological order and the quantum spin Hall effect. *Physical Review Letters* **95**, 146802 (2005).
[26] Bernevig, B. A., Hughes, T. L. & Zhang, S.-C. Quantum Spin Hall Effect and Topological Phase Transition in HgTe Quantum Wells. *Science* **314**, 1757–1761 (2006).
[27] Moore, J. E. & Balents, L. Topological invariants of time-reversal-invariant band structures. *Physical Review B* **75**, 121306 (2007).
[28] Fu, L., Kane, C. L. & Mele, E. J. Topological Insulators in Three Dimensions. *Physical Review Letters* **98**, 106803 (2007).
[29] Hasan, M. Z. & Kane, C. L. Colloquium: Topological insulators. *Reviews of Modern Physics* **82**, 3045–3067 (2010).
[30] Qi, X.-L. & Zhang, S.-C. Topological insulators and superconductors. *Reviews of Modern Physics* **83**, 1057–1110 (2011).
[31] Su, W. P., Schrieffer, J. R. & Heeger, A. J. Solitons in Polyacetalene. *Physical Review Letters* **42**, 1698 (1979).
[32] Nakahara, M. *Geometry, Topology and Physics* (Hilger, Bristol, 1990).
[33] Dirac, P. A. M. The Quantum Theory of the Electron. *Royal Society of London Proceedings Series A* **117**, 610–624 (1928).
[34] Witten, E. Dynamical breaking of supersymmetry. *Nuclear Physics B* **188**, 513 – 554 (1981).
[35] Cooper, F., Khare, A. & Sukhatme, U. Supersymmetry and quantum mechanics. *Physics Reports* **251**, 267 – 385 (1995).
[36] Schnyder, A. P., Ryu, S., Furusaki, A. & Ludwig, A. W. W. Classification of topological insulators and superconductors in three spatial dimensions. *Physical Review B* **78**, 195125 (2008).
[37] Jackiw, R. & Rebbi, C. Solitons with Fermion Number 1/2. *Physical Review D* **13**, 3398–3409 (1976).
[38] Volovik, G. E. *The Universe in a Helium Droplet* (Clarenden, Oxford, 2003).
[39] Haldane, F. D. M. & Raghu, S. Possible Realization of Directional Optical Waveguides in Photonic Crystals with Broken Time-Reversal Symmetry. *Physical Review Letters* **100**, 013904 (2008).
[40] Wang, Z., Chong, Y. D., Joannopoulos, J. D. & Soljačić, M. Reflection-Free One-Way Edge Modes in a Gyromagnetic Photonic Crystal. *Physical Review Letters* **100**, 013905 (2008).
[41] Prodan, E. & Prodan, C. Topological Phonon Modes and Their Role in Dynamic Instability of Microtubules. *Physical Review Letters* **103**, 248101 (2009).
[42] Berg, N., Joel, K., Koolyk, M. & Prodan, E. Topological phonon modes in filamentary structures. *Physical Review E* **83**, 021913 (2011).
[43] Callias, C. Axial Anomalies and Index Theorems on Open Spaces. *Communications in Mathematical Physics* **62**, 213–234 (1978).
[44] Bott, R. & Seeley, R. Some Remarks on Paper of Callias. *Communications in Mathematical Physics* **62**, 235–245 (1978).
[45] Hirayama, M. & Torii, T. Fermion Fractionalization and Index Theorem. *Progress of Theoretical Physics* **68**, 1354–1364 (1982).
[46] Niemi, A. J. & Semenoff, G. W. Fermion Number Fractionalization in Quantum Field Theory. *Physics Reports* **135**, 99–193 (1986).
[47] Lakes, R. Foam Structures with a Negative Poisson's Ratio. *Science* **235**, 1038–1040 (1987).
[48] Lawler, M. J. Emergent gauge dynamics of highly frustrated magnets. *New Journal of Physics* **15**, 043043 (2013).

SUPPLEMENTARY ONLINE MATERIALS

Proof of Index Theorem

In this appendix we provide details of the proof of the index theorem discussed in the text. Our starting point is equation (4), which describes the zero-mode count in a region S of a larger system. Using the fact that $\{H, \tau^z\} = [\rho_S(\hat{\mathbf{r}}), \tau^z] = 0$ it is straightforward to check that equations (3-5) imply that

$$\nu_T^S = \frac{1}{2} \lim_{\epsilon\to 0} \mathrm{Tr}\left[\tau^z \frac{1}{\mathcal{H}+i\epsilon}[\rho^S(\hat{\mathbf{r}}), \mathcal{H}]\right]. \tag{15}$$

Since $[\rho^S, \mathcal{H}] = 0$ for $\rho_S = 1$, and $\mathcal{H}$ has a finite range a, ν_T^S comes only from the boundary of region S where $\rho^S(\mathbf{r})$ varies. If we assume that the boundary region is gapped and that $\rho(\mathbf{r})$ varies slowly on the scale $L \gg a$, then we safely take ϵ to zero and expand to leading order in a/L. Since $[\rho^S(\hat{\mathbf{r}}), \mathcal{H}]_{\alpha\beta} = \mathcal{H}_{\alpha\beta}(\rho^S(\mathbf{r}_\alpha) - \rho^S(\mathbf{r}_\beta)) \sim \mathcal{H}_{\alpha\beta}(\mathbf{r}_\alpha - \mathbf{r}_\beta)\cdot \nabla\rho(\mathbf{r}_\beta)$, we may write

$$\nu_T^S = \frac{1}{2}\mathrm{Tr}\left[\tau^z \nabla\rho(\hat{\mathbf{r}})\cdot \mathcal{H}^{-1}[\hat{\mathbf{r}}, \mathcal{H}]\right]. \tag{16}$$

We next suppose that in the boundary region the lattice is periodic, so that the trace may be evaluated in a basis of plane waves:

$$|\mathbf{k}, a\rangle = \frac{1}{\sqrt{N}} \sum_{\mathbf{R}} \exp i\mathbf{k}\cdot(\mathbf{R}+\mathbf{d}_a)|\mathbf{R}+\mathbf{d}_a\rangle, \tag{17}$$

where $\mathbf{R}$ is a Bravais lattice vector in a system with periodic boundary conditions and N unit cells. $\mathbf{d}_a$ are basis vectors for the $dn_s + n_b$ sites and bonds per unit cell. The phases are chosen such that the position operator is $\hat{\mathbf{r}} \sim i\nabla_{\mathbf{k}}$. In this basis, the Bloch Hamiltonian $\mathcal{H}(\mathbf{k})$ is a $dn_s + n_b$ square matrix with off diagonal blocks $Q(\mathbf{k})$ and $Q^\dagger(\mathbf{k})$, where

$$Q_{ab}(\mathbf{k}) = \langle \mathbf{k}, a|Q|\mathbf{k}, b\rangle. \tag{18}$$

ν_T^S then has the form

$$\nu_T^S = \int_{\partial S} d^{d-1}S\, \mathbf{P}_T\cdot\hat{n} \tag{19}$$

where the integral is over the boundary of S with inward normal $\hat{n}$, and

$$\mathbf{P}_T = \int_{BZ} \frac{d^d\mathbf{k}}{(2\pi)^d} \mathrm{Im}\ \mathrm{Tr}[Q^{-1}\nabla_{\mathbf{k}} Q]. \tag{20}$$

It is useful, to write

$$\mathrm{Im}\mathrm{Tr}[Q^{-1}\nabla_{\mathbf{k}}Q] = \nabla_{\mathbf{k}}\mathrm{Im}\log\det Q. \tag{21}$$

It is then straightforward to show that

$$\det Q(\mathbf{k}+\mathbf{G}) = \det Q(\mathbf{k})\exp[-i\mathbf{G}\cdot\mathbf{r}_0], \tag{22}$$

where

$$\mathbf{r}_0 = d\sum_{\text{sites } i}\mathbf{d}_i - \sum_{\text{bonds } m}\mathbf{d}_m. \tag{23}$$

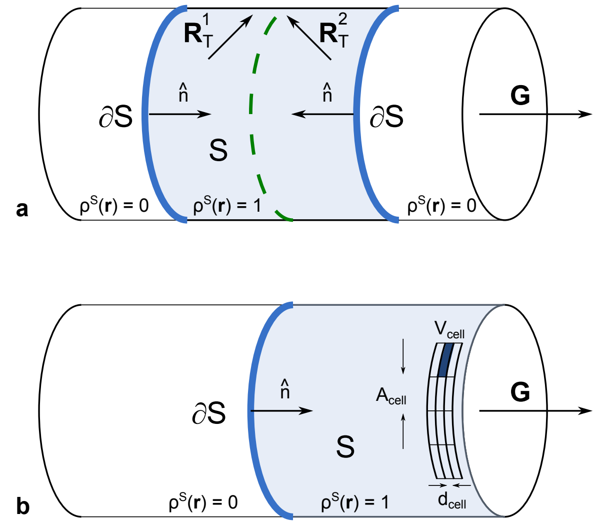

FIG. 1: **Evaluating the zero mode count. a** Cylindrical geometry for evaluating the zero mode count for a domain wall between $\mathbf{R}_T^1$ and $\mathbf{R}_T^2$, indicated by the dashed line. **b** Cylindrical geometry for evaluating the zero mode count for a surface indexed by reciprocal lattice vector $\mathbf{G}$. The region S covers half the cylinder. The boundary ∂S is deep in the interior. **b** also shows our notation for the surface unit cell.

For a general lattice, $\mathbf{r}_0$ is non zero. However, if the coordination number of site i is z_i then $\mathbf{r}_0 = \sum_i(d - z_i/2)\mathbf{d}_i + \mathbf{R}$, where $\mathbf{R}$ is a Bravais lattice vector. Thus, for an isostatic lattice with uniform coordination $z = 2d$, $\mathbf{r}_0$ is a Bravais lattice vector, and it is always possible to shift $\mathbf{d}_m$ by lattice vectors to make $\mathbf{r}_0 = 0$. In the text of the paper, we assumed $\mathbf{r}_0 = 0$. Here we will keep it general, and show that while $\mathbf{r}_0$ affects ν_T^S, its effect is canceled by a compensating term in ν_L^S.

For the general case, let us write $\det Q(\mathbf{k}) = q_0(\mathbf{k})\exp[-i\mathbf{k}\cdot\mathbf{r}_0]$, where $q_0(\mathbf{k}) = q_0(\mathbf{k}+\mathbf{G})$ is periodic in the BZ. Equation (20) then involves two pieces:

$$\mathbf{P}_T = \frac{1}{V_{\rm cell}}\left[-\mathbf{r}_0 + \mathbf{R}_T\right]. \tag{24}$$

Here $\mathbf{R}_T$ is a Bravias lattice vector describing the winding numbers of the phase of $q_0(\mathbf{k})$ around the cycles of the BZ. It may be written $\mathbf{R}_T = \sum_i n_i\mathbf{a}_i$ with

$$n_i = \frac{1}{2\pi i}\int_{C_i} d\mathbf{k}\cdot\nabla_{\mathbf{k}}\log q_0(\mathbf{k}) \tag{25}$$

where as in the text, we assume that for a given cycle C_i of the BZ the winding number is path indpendent.

Application to zero modes at a domain wall

To determine the zero mode count at a domain wall between topological states $\mathbf{R}_T^1$ and $\mathbf{R}_T^2$, we consider a cylinder perpendicular to the domain wall (or a similar construction for d dimensions). We expect the zero mode count to be proportional to the "area" A (or length in 2D) of the domain wall. We will, therefore, be interested in the zero mode count per unit cell, $\nu^S/N_{\rm cell}$, where $N_{\rm cell} = A/A_{\rm cell}$, and $A_{\rm cell} = V_{\rm cell}/d_{\rm cell}$ is the projected area of the surface unit cell, which can be expressed in terms of the volume of the bulk unit cell $V_{\rm cell}$ and the distance $d_{\rm cell}$ between Bragg planes. Referring to Supplementary Fig. 1a, we use equation (24) to evaluate equation (19) away from the domain wall to give $\nu_T = (A/V_{\rm cell})(\mathbf{R}_T^1 - \mathbf{R}_T^2)\cdot\hat{n}$, where $\hat{n}$ is the unit vector pointing to the right. The zero mode count per unit cell can be expressed in terms of the reciprocal lattice vector $\mathbf{G} = 2\pi\hat{n}/d_{\rm cell}$ that indexes the domain wall as

$$\nu_T^S/N_{\rm cell} = \mathbf{G}\cdot(\mathbf{R}_T^1 - \mathbf{R}_T^2)/2\pi. \tag{26}$$

Application to zero modes at the edge

We next determine the number of zero modes localized on a surface (or edge in 2d) indexed by a reciprocal lattice vector $\mathbf{G}$. Consider a cylinder with axis perpendicular to $\mathbf{G}$ and define the region S to be the points nearest to one end of the cylinder, as shown in Supplementary Fig. 1b. A similar construction can be used to count the zero modes on a surface in d dimensions.

ν_T^S is determined by evaluating equation (6) deep in the bulk of the cylinder where the lattice is periodic. From equation (20) we may write

$$\nu_T^S/N_{\rm cell} = \mathbf{G}\cdot(\mathbf{R}_T - \mathbf{r}_0)/2\pi. \tag{27}$$

The local count, ν_L^S, depends on the details of the termination at the surface and is given by the macroscopic "surface charge" that arises when positive charges $+d$ are placed on the sites and negative charges -1 are placed on the bonds. As discussed in the text, it can be determined by evaluating the dipole moment of a unit cell with site and bond vectors $\tilde{\mathbf{d}}_a$ that is defined so that the surface can be accomodated with no left over sites or bonds. This unit cell is in general different from the unit cell used to compute ν_T^S, and its dipole moment is in general not quantized. However, since the difference is due to a redefinition of which bond is associated with which unit cell, the dipole moment differs from $\mathbf{r}_0$ by a Bravais lattice vector,

$$\mathbf{R}_L = d\sum_{\text{sites } i}\tilde{\mathbf{d}}_i - \sum_{\text{bonds } m}\tilde{\mathbf{d}}_m - \mathbf{r}_0. \tag{28}$$

It follows that the local count may be written

$$\nu_L^S/N_{\rm cell} = \mathbf{G}\cdot(\mathbf{R}^L + \mathbf{r}_0)/2\pi. \tag{29}$$

The total zero mode count on the edge is then

$$\nu^S/N_{\rm cell} = \mathbf{G}\cdot(\mathbf{R}^L + \mathbf{R}^T)/2\pi. \tag{30}$$

It can be seen that the dependence on $\mathbf{r}_0$, which depends on the arbitrary unit cell used to define ν_T^S cancels.